

REGULAR PAPER

High-power broad-area laser diode performance improvement with a double pedestal structure

To cite this article: Younghyun Kim *et al* 2019 *Jpn. J. Appl. Phys.* **58** 042004

View the [article online](#) for updates and enhancements.



High-power broad-area laser diode performance improvement with a double pedestal structure

Younghyun Kim, Jung-Tack Yang, and Woo-Young Choi*

Department of Electrical and Electronic Engineering, Yonsei University, Seoul 120-749, Republic of Korea

*E-mail: wchoi@yonsei.ac.kr

Received November 14, 2018; revised February 26, 2019; accepted February 26, 2019; published online March 28, 2019

We propose a novel heat-sinking structure for a high-power broad-area laser diode. In our laser diode, the pedestal structure is introduced to both top and bottom sides of the laser diode so that the heat generated within the device can be more efficiently released. The characteristics of high-power broad-area laser diodes containing the double pedestal structure are numerically analyzed by self-consistent electro-thermal-optical simulation. It is demonstrated that our laser diode has narrower lateral far-field angle and lower active region temperature compared to previously reported high-power laser diode structures. © 2019 The Japan Society of Applied Physics

1. Introduction

High-power broad-area semiconductor laser diodes are widely used as the pumping source for various types of high-power lasers for military, industrial, commercial, and consumer applications due to their advantages in high efficiency, low cost, and small size.^{1–3} However, their performances can suffer from self-heating, which causes the thermal rollover resulting in the limited maximum output power and the far-field blooming causing the reduced pump beam coupling efficiency.⁴ Previous studies have shown that thermal lensing^{5–8} due to the lateral refractive index gradient causes generation of higher-order lateral modes and narrowing of the near-field profile of each guided mode resulting in the far-field blooming.^{9–12} In order to solve this problem, the pedestal heat-sinking structure has been demonstrated for reducing the far-field blooming^{13,14} and numerically analyzed.¹⁵

However, with this pedestal structure, the active region temperature is actually higher than without it, resulting in the lower slope efficiency and the thermal rollover at the lower current. In order to achieve reduced far-field blooming without increasing the active region temperature, a more efficient method of releasing heat generated in the active region to the heat sink is needed. We have proposed such a broad-area laser diode in which the substrate is removed by epitaxial liftoff and a heat sink is connected to the bottom side as well as the top side for efficient heat-sinking.¹⁶ The epitaxial liftoff technique can be used to remove the substrate^{17,18} and has been demonstrated for various semiconductor devices of high electron mobility transistors, heterojunction phototransistors, solar cells,^{19,20} light emitting diodes,²¹ and laser diodes.²² In this paper, for further improvement, we propose the double pedestal (DP) structure in which the pedestal structure is introduced to the both sides of the previously reported structure¹⁶ and report its enhanced characteristics obtained with numerical simulation.

This paper is organized as follows. In Sect. 2, we explain the simulation method used for our investigation and verify its accuracy. Section 3 presents the performance comparison of laser diodes with and without the top pedestal structure. Section 4 explains the DP structure and its fabrication method, and Sect. 5 presents the improved performance of a high-power laser diode with the DP structure. Section 6 concludes the paper.

2. Simulation method and its verification

For the numerical analysis of high-power laser diodes, we employ the commercially available simulator LASTIP,²³ which can self-consistently simulate laser diode electro-thermal-optical properties including transport of electrons and holes, quantum well optical gain, and heat flow in the transverse plane. For heat sources, Joule heat and heat due to optical modal absorption and non-radiative recombination are considered. In order to verify its accuracy, we first simulate a high-power laser diode whose structure is described in a published paper.²⁴ The 852 nm laser diode is composed of a compressively strained 8 nm thick $\text{Ga}_{0.9}\text{In}_{0.1}\text{As}_{0.9}\text{P}_{0.1}$ single quantum well embedded between 500 nm thick $\text{Ga}_{0.5}\text{In}_{0.5}\text{P}$ separate confinement (SCH) layers and $\text{Al}_{0.2}\text{Ga}_{0.2}\text{In}_{0.6}\text{P}$ P- and N-type cladding layers. It has a 100 μm wide rib and a 2000 μm long cavity with facet reflectivities of 5% and 95%. The details of mole fractions are not given in the paper, but In and P fractions of the single quantum well are estimated for 852 nm lasing wavelength, and SCH and cladding layers are assumed lattice-matched to the GaAs substrate.

Figure 1(a) shows the vertical profile of the bandgap diagram at equilibrium. The refractive indices for various layers at 852 nm are obtained from linear interpolation based on values given in Refs. 25–26 as shown in Fig. 1(b). For thermal simulation, the thermal conductivity of each semiconductor layer is given by the Ref. 27. As the thermal lens effect is suppressed by the pedestal structure having different thermal conductivities above and at the side of the rib, the numerical values of thermal conductivities are important for this simulation work. Thermal conductivity of 200 W mK^{-1} is used for the metal (CuW) above the rib and 1.5 W mK^{-1} for the dielectric layer (SiO_2) at the side of the rib. The temperatures at the very top metal above the rib waveguide and the very bottom metal below the 300 μm thick GaAs substrate are assumed to remain at the heat sink temperatures of 293 K. It is important to consider the thermal index change for SCH layers, because it is the main cause for the far-field blooming. For this, we use $2.0 \times 10^{-4} \text{ K}^{-1}$ as the temperature dependence of the thermal index change for GaInP.²⁸ Also, free-carrier absorption and carrier-induced refractive index change are taken into account. Then, transversal lasing modes are calculated self-consistently by the perturbed refractive index profile from the Helmholtz equation. In

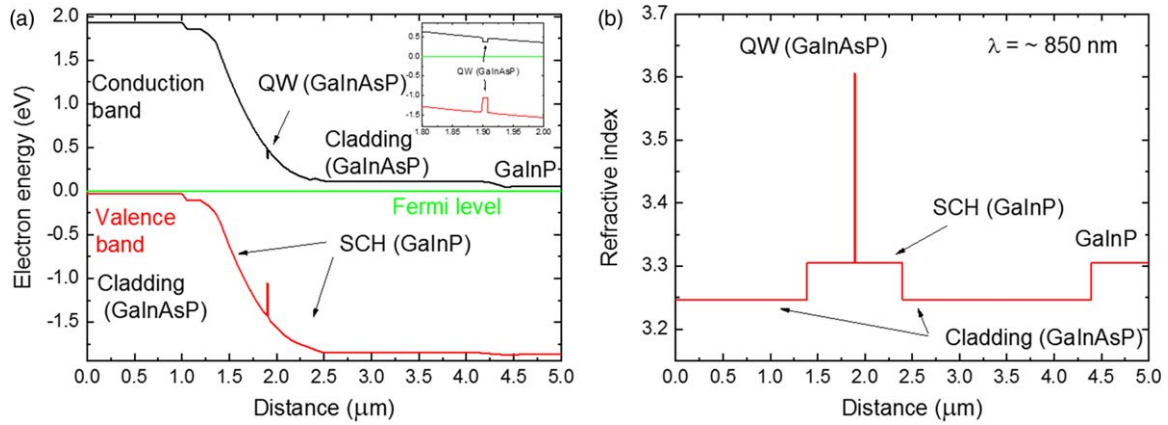


Fig. 1. (Color online) Vertical profiles of (a) bandgap diagram with enlarged QW region (inset) and (b) refractive indices near 850 nm used for device simulation.

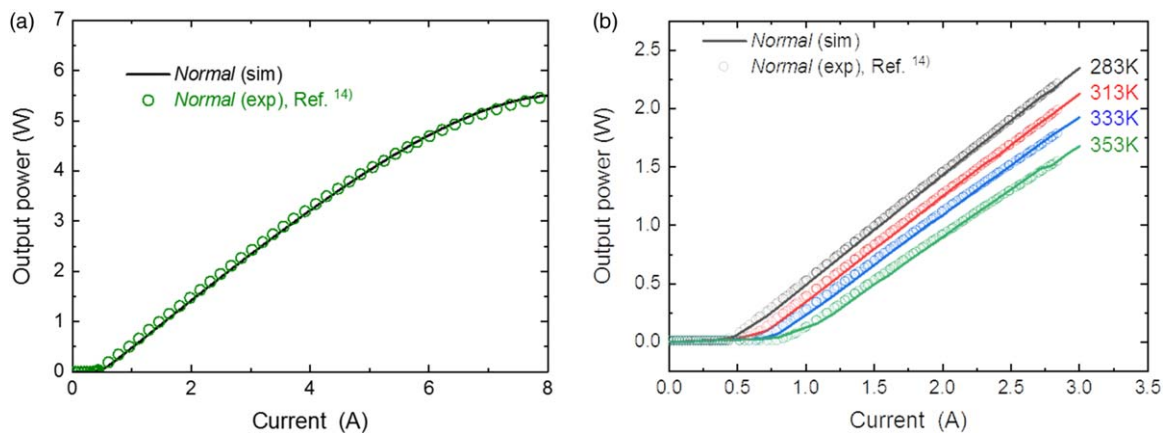


Fig. 2. (Color online) Output laser power versus injected current (a) with 0–8 A at 293 K and (b) with 0–3 A at variable temperature conditions.

order to reproduce the experiment results shown in Fig. 2 of the Ref. 24, we use the Shockley–Read–Hall carrier lifetime of 6 ns, Auger coefficient of $1 \times 10^{-29} \text{ cm}^6 \text{ s}^{-1}$ for the quantum well, and the internal loss of 2.9 cm^{-1} as fitting parameters. Figure 2 shows the simulated (lines) and the experiment (circles) L – I characteristics for the laser diode structure described above. Figure 2(a) is the result for the injected current ranging from 0 to 8 A at 293 K and Fig. 2(b) is the result from 0 to 3 A in various temperature conditions. As can be seen, the simulation results agree well with the measurement results. Figure 3 shows the vertical and lateral far-field profiles. As shown in Fig. 3(a), the vertical far-field profiles of the simulation and the experiment show very good agreement, which is relatively simple to determine because only one single mode exists vertically and this does not have much dependence on injected currents. Figure 3(b) shows the lateral far-field profiles of the simulated and the measured results at 3 A. Although the simulation result shown with the black line is slightly narrower than experimental result shown in green circles, they show reasonably good agreement. These simulation conditions are used for other structures, as will be described in Sect. 3.

3. Comparison of laser diode performance with and without the pedestal structure

In this section, we present the comparison of laser diode performance with the normal and the pedestal structures as shown in the left (Normal) and right (Pedestal) insets of

Fig. 4(a), respectively. The normal structure is same as the structure simulated in Sect. 2. The pedestal structure has identical layers but with a top pedestal structure as shown in the Refs. 13, 14, 29 and the inset in the Fig. 4(a). The contact size above the rib of the pedestal structure is same as $100 \mu\text{m}$ wide rib. For the normal structure, the thermal flow is provided in the entire top region but for the pedestal structure, only in the rib region due to the insulator having much lower thermal conductivity than the metal. The red and the dashed red lines in Fig. 4(a) show the simulated L – I characteristics and the quantum well temperature for the pedestal structure, respectively. Also, the simulated lateral far-field for the pedestal structure is shown by the red line in Fig. 4(b). As expected, the lateral far-field of the pedestal structure is narrower, but its quantum well temperature is higher than that of the normal structure, resulting in the thermal rollover at the lower current compared to the normal structure.

Figures 5(a) and 5(b) show the quantum well temperature and refractive index at the top SCH layer as a function of distance from the center to the edge along x -axis as depicted in the insets of Fig. 4(a). With the pedestal structure, the differences in temperature and the refractive index for the center and edge regions are reduced as can be seen in Figs. 5(a) and 5(b); therefore, the lateral far-field becomes narrower as shown in Fig. 4(b). These results qualitatively agree with the previously reported results.²⁹⁾ However, the inverse thermal lens effect shown in Figs. 2 and 3 of the

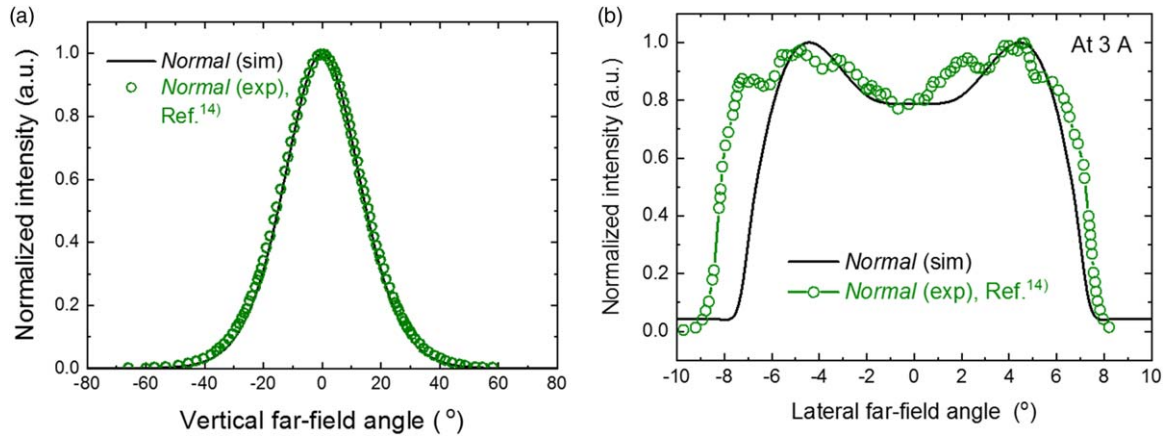


Fig. 3. (Color online) (a) Vertical and (b) lateral far-field profiles.

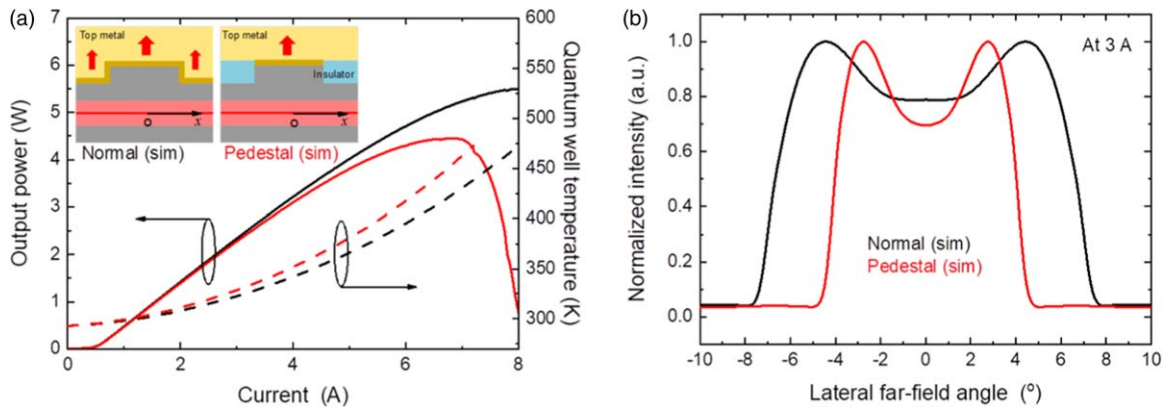


Fig. 4. (Color online) (a) Output laser power versus injected current and (b) lateral far-field profile of Normal and Pedestal.

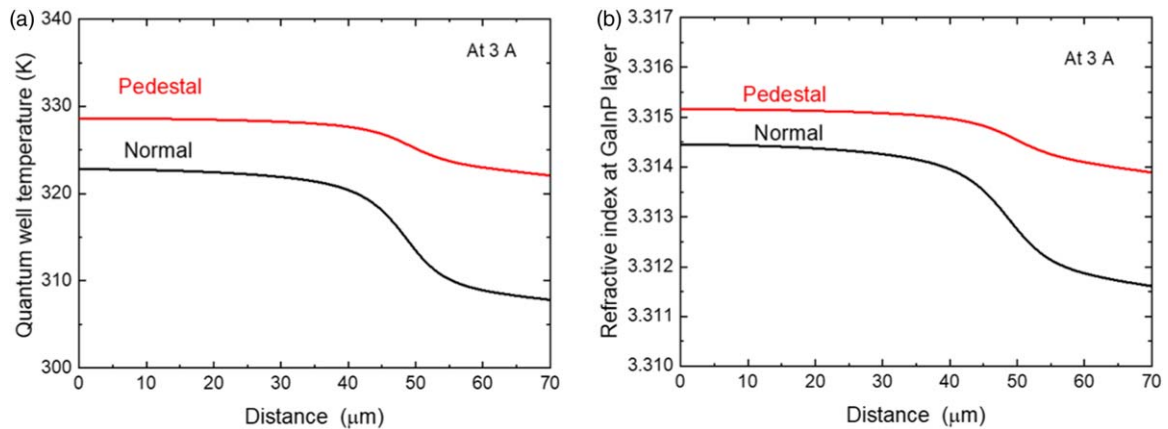


Fig. 5. (Color online) (a) Quantum well temperature and (b) refractive index at GaInP SCH layer of Normal and Pedestal.

Ref. 29 is not observed. It is difficult to quantitatively compare them because the laser diode and pedestal structures as well as the materials are different. However, since they show the same trend in which the pedestal structure suppresses the thermal lens effect, we believe it would also show the inverse thermal lens effect when the pedestal structure is optimally designed with the two different thermal conductivities.

4. Fabrication method for the DP structure

Figure 6 presents the fabrication process for our high-power laser diode with the epitaxial liftoff technique. It starts with a high-power broad-area laser diode having an insulator for the

pedestal structure as shown in Fig. 6(a). However, unlike the conventional laser diodes for which the facets are fabricated by cleaving, the facets for our laser diodes are formed by dry etching and subsequent passivation^{22,30} because the substrate will be removed. In addition, it has an AlAs sacrificial layer and a GaAs etch stop layer embedded between the N-cladding and the GaAs substrate for the epitaxial liftoff process. A metal substrate is bonded to the fabricated laser diode by the wafer bonding technique as shown in Fig. 6(b). Then, the GaAs substrate is removed by etching the AlAs sacrificial layer as shown Fig. 6(c), followed by formation of the N-contact metal layer and the insulator layer needed for the bottom pedestal structure as shown in Fig. 6(d). Then, the

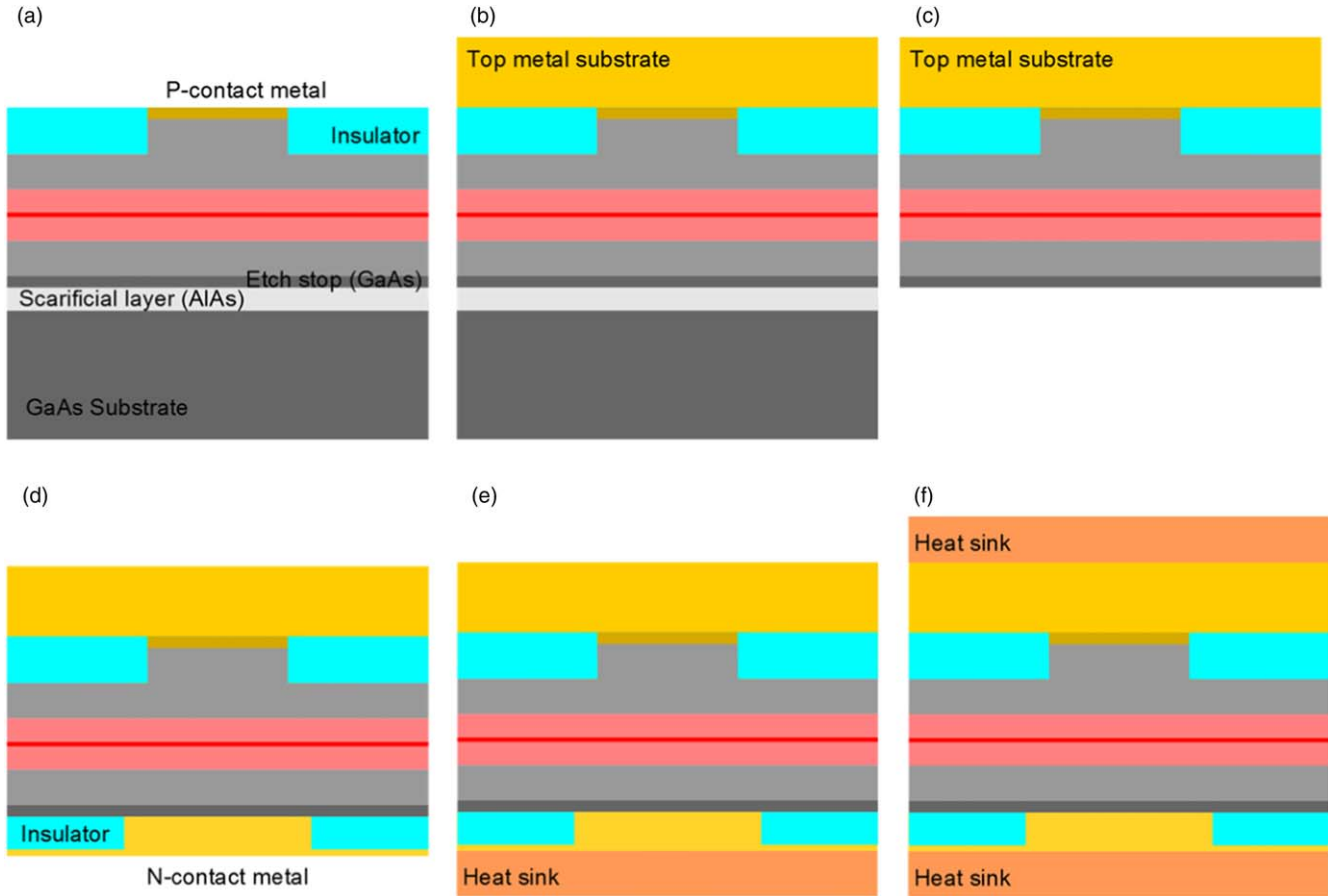


Fig. 6. (Color online) Fabrication process flow for DP structure: (a) high-power laser diode with an insulator for the pedestal structure, (b) wafer bonding of the laser diode substrate and the top metal substrate, (c) removal of GaAs substrate by epitaxial liftoff, (d) construction of the bottom pedestal structure with an insulator and an N-contact metal, (e) formation of bottom heat sink, and (f) formation of top heat sink.

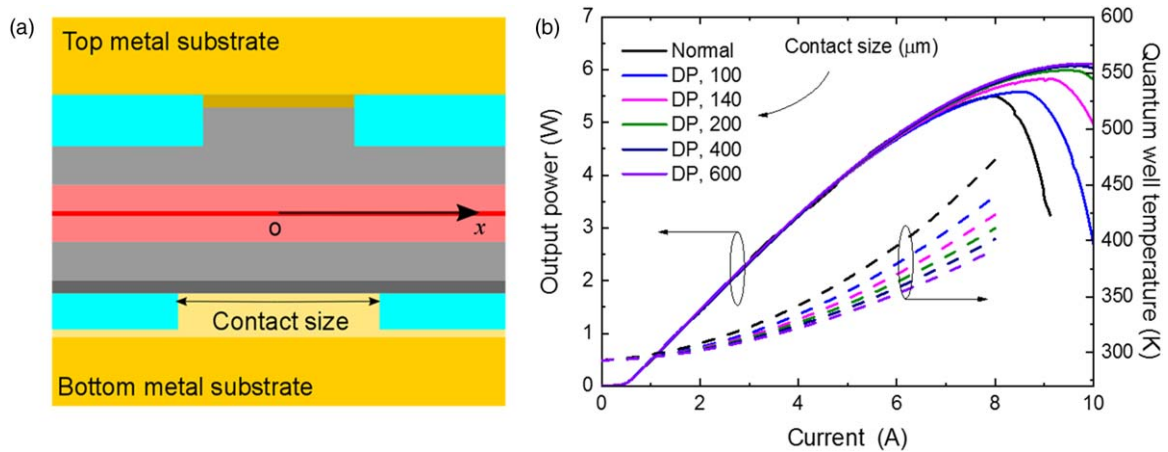


Fig. 7. (Color online) (a) Cross section of DP structure and (b) output laser power versus injected current for Normal and DP structures for various contact sizes of 100, 140, 200 and 600 μm .

substrate is diced and each high-power laser diode or diode bar is mounted on the heat sink, as shown in Fig. 6(e). Finally, the heat sink is also connected to the top metal substrate. In this structure, the heat generated in the active region can be released above and below the active region thanks to the removal of the bulk substrate and heat sinks connected to both sides. For analyzing the DP structure, the conditions of the top and bottom metals, the insulators, and the heat sink temperatures are assumed to be those described in Sect. 2.

5. Numerical analysis of the DP structures

We simulate the device performance of the DP structure shown in Fig. 7(a). Figure 7(b) shows the L - I characteristics in the current range of 0–10 A at the heat sink temperatures of 293 K with the various contact sizes of 100, 140, 200, and 600 μm . The quantum well temperature decreases with the increasing contact size because the larger contact size reduces the thermal resistance, resulting in the higher slope efficiency and thermal rollover at the higher current.

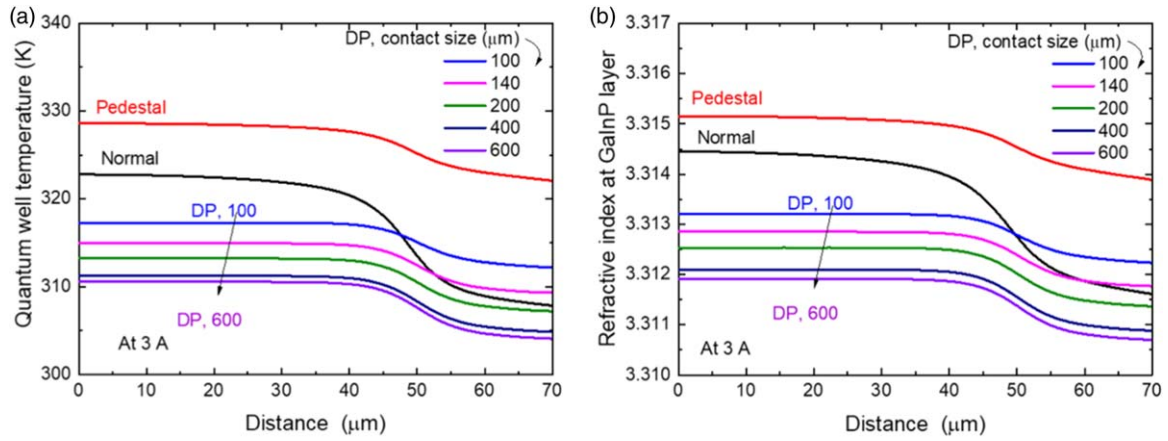


Fig. 8. (Color online) (a) Quantum well temperature and (b) refractive index at GaInP SCH layer of Normal, Pedestal and DP structures for various contact sizes.

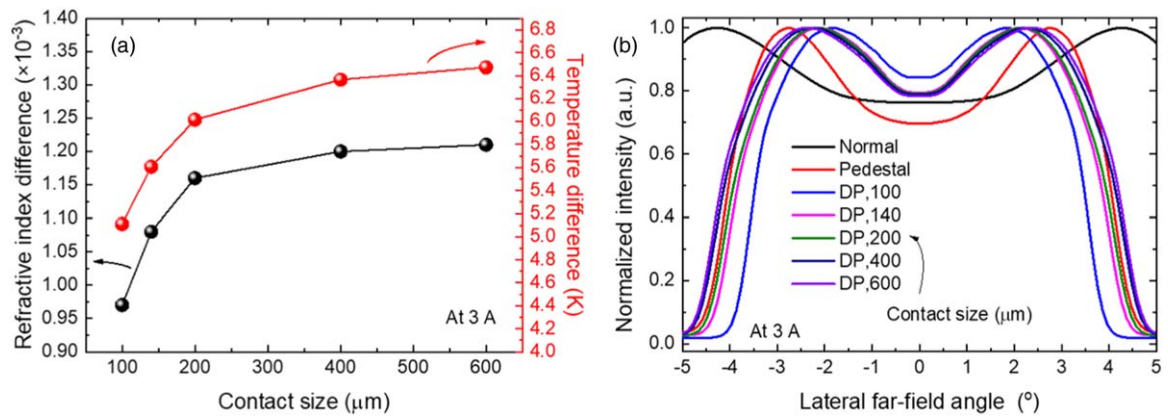


Fig. 9. (Color online) (a) Differences in refractive index and temperature versus contact size, and (b) half-width lateral far-field profile for Normal, Pedestal, and DP structures.

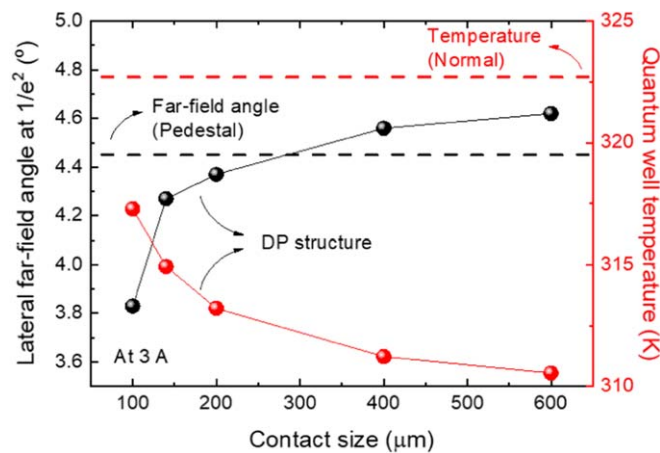


Fig. 10. (Color online) Half-width lateral far-field angle at $1/e^2$ of the peak intensity value and quantum well temperature at 3 A for varying contact sizes.

Figures 8(a) and 8(b) show the quantum well temperature and refractive index at the GaInP top SCH layer as a function of distance from the center to the edge along the x -axis as depicted in Fig. 7(a). Compared to the profiles of the normal structure, the temperature and the index as well as their differences decrease due to the DP structure. Figure 9(a) shows the refractive index and temperature differences between at 0 and 70 μm in Figs. 8(a) and 8(b) as a function of the contact size. The differences become smaller with the

decreasing contact size. This results in the narrower lateral far-field profile as shown in Fig. 9(b) because devices with smaller contact sizes experience weaker thermal lens effect. Figure 10 shows the lateral far-field angle at the location where the far-field intensity is $1/e^2$ of the peak value and the quantum well temperature for the contact size. Although the cases of the contact size less than 200 μm show the narrower lateral far-field angle, those of 400 and 600 μm show the larger far-field angle than that of the pedestal structure. This

is because the bottom-side heat-sinking is too strong for the effect of the top pedestal structure to show up. Therefore, it is necessary to design the contact size properly for the DP structure in order to achieve the optimal lateral far-field pattern as well as the reduced quantum well structure.

6. Conclusions

We have proposed the high-power broad-area laser diode with the DP structure, which can be fabricated by removing the bulk substrate and introducing the pedestal structure to the top and bottom of a laser diode. We have numerically demonstrated that the proposed DP structure can achieve both the narrower lateral far-field angle and the lower quantum well temperature compared to previously reported high-power laser diodes.

Acknowledgments

This work was supported by the Research Fund of High Efficiency Laser Laboratory of Agency for Defense Development of Korea (No.UD160069BD).

- 1) L. Zhong and X. Ma, *Optoelectronics—Devices and Applications*, 2011, p. 325.
- 2) V. Gapontsev, N. Moshegov, I. Berezin, A. Komissarov, P. Trubenko, D. Miftakhutdinov, I. Berishev, V. Chuyanov, O. Raisky, and A. Ovtchinnikov, *Proc. SPIE* **10086**, 1008604 (2017).
- 3) A. V. Aluev, A. M. Morozuk, M. S. Kobayakova, and A. A. Chel'nyi, *Quantum Electron.* **31**, 627 (2001).
- 4) P. Crump, S. Böldicke, C. M. Schultz, H. Ekhteraei, H. Wenzel, and G. Erbert, *Semicond. Sci. Technol.* **27**, 045001 (2012).
- 5) H. Li et al., *IEEE Photonics Technol. Lett.* **19**, 960 (2007).
- 6) M. I. Azawe, *Int. J. Phys. Sci.* **8**, 362 (2013).
- 7) A. Isemann and C. Fallnich, *Opt. Express* **11**, 259 (2003).
- 8) H. Wenzel, P. Crump, A. Pietzak, X. Wang, G. Erbert, and G. Trankle, *New J. Phys.* **12**, 085007 (2010).
- 9) J. Piprek, NUSOD, 2012, p. 119.
- 10) J. Piprek, *IEEE J. Quantum Electron.* **45**, 581 (2013).
- 11) G. Sobczak, E. Dabrowska, M. Teodorczyk, K. Krzyzak, J. Kalbarczyk, and A. Malag, *Photonics Lett. Pol.* **5**, 88 (2013).
- 12) J. Piprek and Z. M. S. Li, *Appl. Phys. Lett.* **102**, 221110 (2013).
- 13) J. G. Bai et al., *Proc. SPIE* **7593**, 75931F (2011).
- 14) W. Sun, R. Pathak, G. Campbell, H. Eppich, J. H. Jacob, A. Chin, and J. Fryer, *Proc. SPIE* **8605**, 86050D (2013).
- 15) J. Piprek, *Proc. SPIE* **8619**, 861910 (2013).
- 16) Y. Kim, Y. Sung, J. Yang, and W. Choi, *Proc. SPIE* **10514**, 105140C (2018).
- 17) P. Demeester, I. Pollentier, P. D. Dobbelaere, C. Brys, and P. V. Daele, *Semicond. Sci. Technol.* **8**, 1124 (1993).
- 18) J. J. Schermer, P. Mulder, G. J. Bauhuis, M. M. A. J. Voncken, J. van Deelen, E. Haverkamp, and P. K. Larsen, *Phys. Status Solidi* **202**, 501 (2005).
- 19) D. M. Geum, M. S. Park, J. Y. Lim, H. D. Yang, J. D. Song, C. Z. Kim, E. Yoon, S. Kim, and W. J. Choi, *Sci. Rep.* **6**, 20610 (2016).
- 20) A. van Geelen, P. R. Hageman, G. J. Bauhuis, P. C. van Rijsingen, P. Schmidt, and L. J. Giling, *Mater. Sci. Eng. B* **45**, 162 (1997).
- 21) F. L. Wu, S. L. Ou, Y. C. Kao, C. L. Chen, M. C. Tseng, F. C. Lu, M. T. Lin, and R. H. Horng, *Opt. Express* **23**, 18156 (2015).
- 22) R. Loi, J. O'Callaghan, B. Roycroft, C. Robert, A. Fecioru, A. J. Trindade, A. Gocalinska, E. Pelucchi, C. A. Bower, and B. Corbett, *IEEE Photonics J.* **8**, 1504810 (2016).
- 23) LASTIP, Crosslight Software Inc., Canada.
- 24) F. J. Vermersch, M. Lecomte, M. Calligaro, O. Parillaud, S. Bansropun, and M. Krakowski, *Proc. SPIE* **5738**, 398 (2005).
- 25) S. Gehrsitz, F. K. Reinhart, C. Gourgon, N. Herres, A. Vonlanthen, and H. Sigg, *J. Appl. Phys.* **87**, 7825 (2000).
- 26) Y. Kaneko and K. Kishino, *J. Appl. Phys.* **76**, 1809 (1994).
- 27) W. Nakwaski, *J. Appl. Phys.* **64**, 159 (1988).
- 28) S. Sokolov, J. Lian, S. Combrie, A. D. Rossi, and A. P. Mosk, *Appl. Opt.* **56**, 3219 (2017).
- 29) J. Piprek, *IEEE Photonics Technol. Lett.* **25**, 958 (2013).
- 30) E. Deichsel and G. Franz, *J. Vac. Sci. Technol. A* **22**, 2201 (2004).